PNAS RESEARCH ARTICLE | CHEMISTRY

Interfacial engineering of plasmonic nanoparticle metasurfaces

Shikai Deng[a], Jeong-Eun Park[a], Gyeongwon Kang[a], Jun Guan[a], Ran Li[b], George C. Schatz[a], and Teri W. Odom[a,b,1]

Edited by Stephan Link, Rice University, Houston, TX; received February 12, 2022; accepted April 22, 2022 by Editorial Board Member Peter J. Rossky

This paper reports how the interfacial engineering of plasmonic nanoparticle (NP) lattices with desired surface characteristics can control plasmon-molecule interactions for tunable nanolasing thresholds. Compared to bare Cu NP lattices, graphene-coated Cu NPs surrounded by aromatic dye molecules gain support lasing with lower thresholds and at lower dye concentrations. This lasing enhancement is attributed to favorable molecular arrangements in electromagnetic hotspots through π–π interactions between graphene and IR-140 (5,5′-dichloro-11-diphenylamine-3,3′-diethyl-10,12-ethylene-thiatricarbocyanine-perchlorate) and 4-(dicyanomethylene)-2-methyl-6-(4-dimethylaminostyryl)-4H-pyran (DCM) dyes. Besides the chemical interactions mediated by few-layer graphene, nanoscale dielectric layers such as fluoropolymer and alumina can also tailor the thresholds by modifying the spatial overlap of the dye near the NP surface. Our work lays the foundation for interfacial engineering of the surface of resonator units in plasmonic metasurfaces for exquisite control of light-matter interactions.

nanolasing | light-matter interactions | Cu plasmonics | graphene | core-shell nanoparticles

Significance

Molecules interacting with metallic nanostructures can show tunable exciton-plasmon coupling, ranging from weak to strong. One factor that influences the interactions is the spatial organization of the molecules relative to the localized plasmon-enhanced electromagnetic fields. In this work, we show that the arrangement of aromatic dye molecules can be tuned within plasmonic hotspots by interfacial engineering of nanoparticle surfaces. By controlling the local chemical and physical interactions, we could modulate lasing thresholds. Surface-functionalized plasmonic metasurfaces open prospects for programmable light-matter interactions at the nanoscale.

Optical metasurfaces are engineered planar structures of dielectric or plasmonic building blocks that can control the propagation of light (1, 2). All-dielectric metasurfaces can support strong Purcell enhancements and photonic resonances with high quality factors ($Q > 10^5$) because of low losses from absorption (3, 4). Compared to dielectric resonators that confine optical fields within their high refractive index materials (5, 6), plasmonic nanostructures squeeze light into subwavelength volumes at their metal-dielectric interfaces (7–10). When metallic nanoparticles (NPs) are diffractively coupled in a periodic array, hybrid photonic-plasmonic modes known as surface lattice resonances (SLRs) form (11, 12). Compared to the localized surface plasmon resonances of single plasmonic NPs, SLRs of NP lattices have higher quality factors ($Q > 400$) and more than an order of magnitude higher near-field enhancements on a per-particle basis (13–15).

Combined with gain media, plasmonic NP lattices can provide optical feedback for lasing (13, 16, 17). Since lasing action is sensitive to the intensity and distribution of optical near fields in cavities, the structural engineering of NP lattices has been exploited for control over a wide range of lasing characteristics (18, 19). For example, polarization-dependent lasing has been demonstrated in lattices of anisotropic NPs (20), and modification of the photonic band structure by varying either the lattice geometry or the refractive index environment can tune the wavelength, direction, and polarization of lasing emission (19, 21–24). Because surface plasmons decay exponentially from metal-dielectric interfaces (8, 13, 25, 26), the spatial overlap of the electromagnetic field and emitter is critical. Although tailoring hotspot locations by combined NP shape and mode engineering (27) and arranging emitters with nanometer precision in colloidal systems (28–33) have shown potential for lasing control, the rational design of plasmon-emitter organization in lithographically fabricated NP lattices is underexplored. Thin-film deposition techniques such as chemical vapor deposition and atomic layer deposition are widely used to create conformal coatings that result in hybrid nanostructures (34). Nanoscale surface layers on plasmonic lattices offer an approach to tune the interfacial interactions between NPs and emitters for exquisite control over lasing action.

Here, we show how surface engineering of plasmonic NP lattices with different functional layers can manipulate nanolasing characteristics. Few-layer graphene conformally grown on arrays of Cu NPs combined with molecular dyes as gain media showed lasing action at lower concentrations and lower thresholds compared to bare Cu NP lattices. We attribute these improvements to π–π interactions between aromatic molecules and graphene, which was confirmed by calculations of adhesion energy and simulations of a surface-dye lasing model. Dielectric fluoropolymer (CF_x) and alumina (Al_xO_y) layers on Cu NPs were also compared as spacers to reduce quenching but showed higher thresholds than graphene of the same thickness. Moreover, increased thicknesses of CF_x layers showed similar lasing behavior, but thicker Al_xO_y layers resulted in higher

Author affiliations: [a]Department of Chemistry, Northwestern University, Evanston, IL 60208; and [b]Department of Materials Science and Engineering, Northwestern University, Evanston, IL 60208

Author contributions: S.D., J.-E.P., and T.W.O. designed research; S.D., J.-E.P., and J.G. performed research; G.K., R.L., and G.C.S. contributed new reagents/analytic tools; S.D., J.-E.P., G.C.S., and T.W.O. analyzed data; and S.D., J.-E.P., J.G., G.C.S., and T.W.O. wrote the paper.

The authors declare no competing interest.

This article is a PNAS Direct Submission. S.L. is a guest editor invited by the Editorial Board.

[1]To whom correspondence may be addressed. Email: todom@northwestern.edu

This article contains supporting information online at http://www.pnas.org/lookup/suppl/doi:10.1073/pnas.2202621119/-/DCSupplemental.

Published May 23, 2022.

thresholds. The materials-dependent thresholds are due to the distinct near-field distributions and intensities that are dominated by the refractive index and weak attractions between F atoms in the CF_x and electron-deficient aromatic rings in the dye molecules.

Results and Discussion

Fig. 1*A* depicts schemes for graphene-encapsulated Cu (Cu@G) and annealed Cu NP square lattices. Cu NP arrays (a_0 = 600 nm) on quartz were prepared by SANE (solvent-assisted nanoscale embossing) and PEEL (photolithography, etching, electron beam deposition, and liftoff) followed by thermal annealing (*SI Appendix*, *SI Methods* and *SI Appendix*, Figs. S1–S3) (14, 35, 36). A modified chemical vapor deposition (CVD) process (14) was used to grow few-layer graphene (~3 nm) on the surface of Cu NPs, which resulted in Cu@G NPs with uniform, domelike shapes (Fig. 1 *B* and *C*). Lattices with optimized diameters (*SI Appendix*, Fig. S4) are predicted to support SLRs around 860 nm; experimentally, these SLRs can support ultranarrow linewidths (4 to 5 nm) (Fig. 1*D*) because of the increased crystallinity, reduced surface roughness, and higher uniformity of NPs in annealed lattices (14). Both types of NP lattices were stored in a dry and inert gas to eliminate surface degradation from the formation of CuO_x.

To determine how few-layer graphene can modulate the interactions between SLRs and emitters, we compared the lasing characteristics from Cu@G and annealed Cu NP lattices as cavities using IR-140 (5,5′-dichloro-11-diphenylamine-3,3′-diethyl-10,12-ethylene-thiatricarbocyanine-perchlorate) dye in dimethyl sulfoxide (DMSO) as gain media (Fig. 2 *A* and *B*). IR-140 molecules have six aromatic rings, and the four that lie in the same plane (highlighted in purple in Fig. 2*A*) are expected to contribute to π–π interactions with graphene (37, 38). Fig. 2*C* depicts NP lattices patterned in the 5 × 5 mm^2 areas used in the measurements. When the NP lattice/dye device structure was pumped with an 800-nm femtosecond (fs)-pulsed laser (1 kHz), lasing was observed at the SLR wavelength (ca. 860 nm) above a threshold (Fig. 2*D*), with emission normal to the lattice plane (a beam divergence of ca. 0.2°) (*SI Appendix*, Fig. S5).

The lasing spectra exhibited clear thresholds and nonlinear increases in intensity with increased pump power for both Cu@G NP lattices (Fig. 2*E*) and Cu NP lattices (*SI Appendix*, Fig. S6). Because gain media at higher concentrations can facilitate lasing action more readily and thus overwhelm local effects at the NP surfaces, we focused on IR-140 solutions with lower concentrations than used in previous work (14). The lasing spectra vs. pump power behavior of the two types of lattices were measured with dye concentrations of 0.4, 0.2, 0.15, and 0.1 mM (*SI Appendix*, Figs. S7–S9). Input-output light-light curves showed that Cu NP lattices support lasing at 0.2 and 0.4 mM, but no lasing was observed with less than 0.15 mM (Fig. 2*F*). In contrast, Cu@G NP lattices supported lasing over the tested range of dye solutions (Fig. 2*G*) and had thresholds lower than Cu NP lattices at the same dye concentrations (Fig. 2*H*). Cu@G NP lattices also showed higher nonlinearities in the input-output light-light curves (*SI Appendix*, Fig. S10), which suggests higher pump absorption efficiencies or lower losses in energy transfer from excited molecules to SLRs with the graphene coating (39). Since both intensity and distribution of the electromagnetic near fields are similar for the two types of lattices (*SI Appendix*, Fig. S11), the lower thresholds of Cu@G NP lattices are likely because of the higher local dye concentrations mediated by π–π interactions between aromatic molecules and few-layer graphene coating (37, 40).

To confirm that graphene contributes to lower thresholds in Cu@G NP lattices, we compared lasing characteristics using gain molecules such as DCM [4-(dicyanomethylene)-2-methyl-6-(4-dimethylaminostyryl)-4H-pyran], which has fewer aromatic rings than IR-140 (two, highlighted in purple in Fig. 3*A*). Lattices with a periodicity of a_0 = 450 nm were used to overlap the wavelength of SLR with the photoluminescence of DCM in DMSO (550 to 700 nm) (Fig. 3*B*). We optimized NP sizes for the fabricated lattices by diameter-sweep calculations (*SI Appendix*, Fig. S12) and then prepared Cu@G NP and annealed Cu NP lattices with narrow SLRs (*SI Appendix*, Fig. S13). Compared to

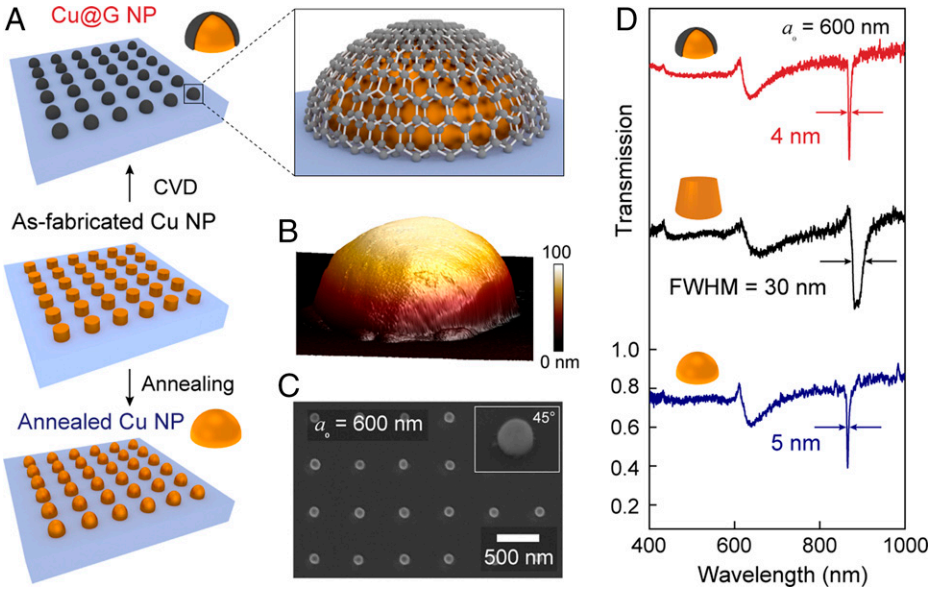

Fig. 1. Preparation of Cu@G NP and annealed Cu NP lattices. (*A*) Schemes of CVD-treated (*Top*), as-fabricated (*Middle*), and annealed (*Bottom*) Cu NP lattices. The zoom-in figure is a schematic Cu@G NP. (*B*) Atomic force microscopy (AFM) three-dimensional image of a single Cu@G NP. (*C*) Scanning electron microscopy (SEM) image of CVD-treated lattices. The inset is a single NP with a 45° tilting angle. (*D*) Transmission spectra of CVD-treated (red), as-fabricated (black), and annealed (blue) Cu NP lattices.

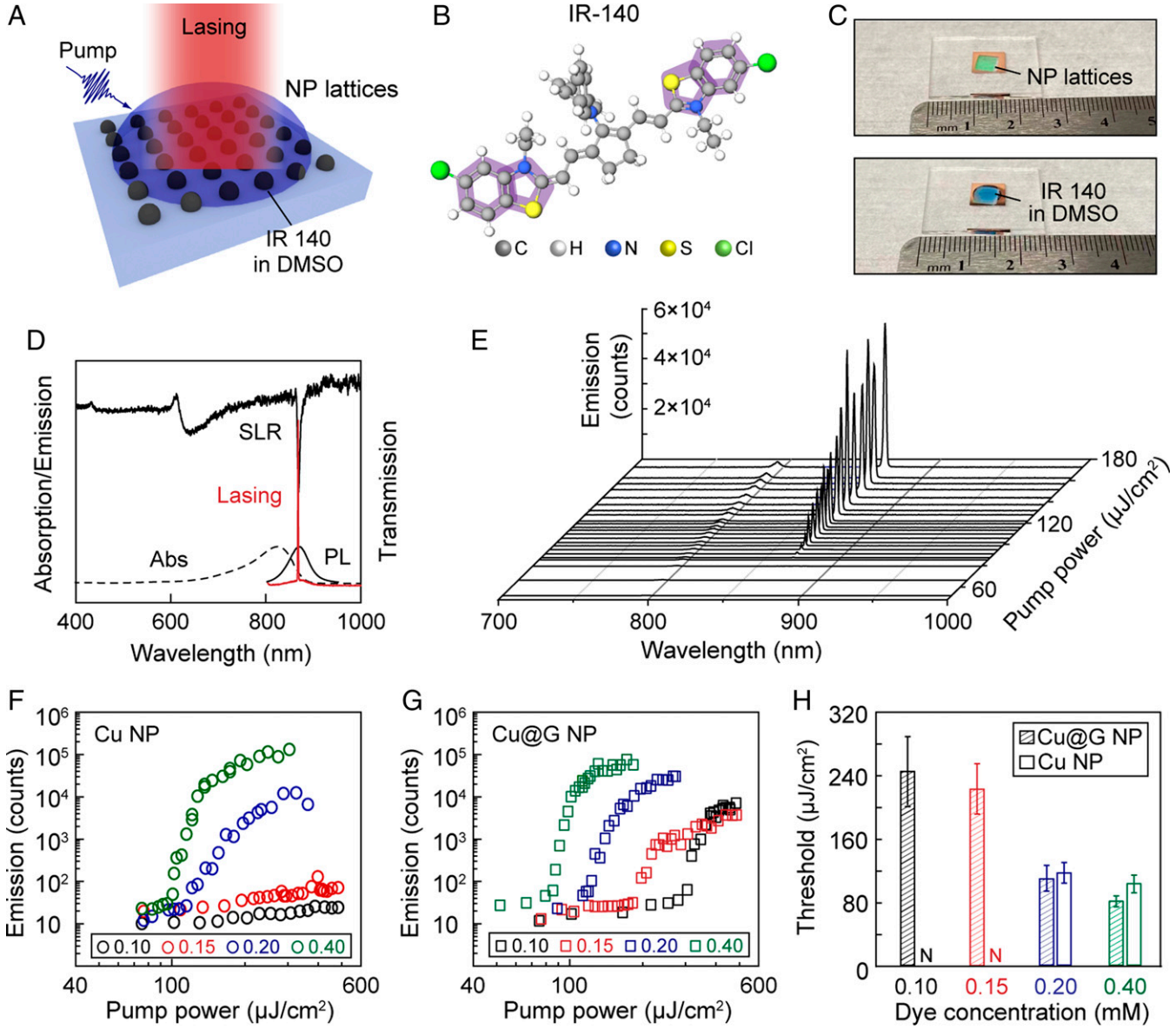

Fig. 2. Graphene modifies lasing behavior of IR-140 dyes in Cu NP lattices. (*A*) Schematic nanolasing of NP lattices with IR-140 in DMSO. (*B*) Three-dimensional ball-and-stick structure of an IR-140 molecule. Purple highlights aromatic rings in the same plane. (*C*) Photos of lattices with and without dye solutions. (*D*) Absorption (Abs) and photoluminescence (PL) of IR-140. SLR spectrally overlaps with PL to generate lasing at a wavelength of 860 nm. (*E*) Waterfall plot of lasing spectra vs. pump intensity for Cu@G NP lattices. Lasing light-light curves of (*F*) annealed Cu and (*G*) Cu@G NP lattices at various IR-140 concentrations on the log-log scale. (*H*) Histogram of thresholds in the light-light curves for both lattices at various IR-140 concentrations. Error bars indicate the SD.

a_0 = 600 nm lattices, SLR peak widths from a_0 = 450 nm lattices were broader since the resonant wavelength is closer to the interband transition of Cu (ca. 600 nm) (*SI Appendix*, Fig. S14).

After pumping the DCM/NP lattice device with a 400-nm fs-pulsed laser (1 kHz), we collected lasing emission normal to the lattice plane ca. 650 nm (Fig. 3*C*) and obtained the lasing spectra at different pump powers (*SI Appendix*, Fig. S15). Both lattices had comparable thresholds at 4 and 5 mM of DCM solutions, but only the Cu@G NP lattices supported lasing at lower concentrations (3 mM) (Fig. 3 *D* and *E*). No lasing was generated for either lattice with dye concentrations lower than 2 mM because of low absorption of DCM at the 400-nm pump wavelength. Different from IR-140, lasing from DCM showed less contrast in both threshold (Fig. 3*F*) and nonlinear increase (*SI Appendix*, Fig. S16) between the Cu@G NP and Cu NP lattices. We attribute the difference to net weaker π–π interactions per DCM molecule compared to IR-140 because of fewer aromatic rings.

Density functional theory (DFT) simulations were performed to understand how graphene can affect the local organization of dyes around the NPs (*SI Appendix*, *SI Methods*). Because graphene increases the adhesion energy between dye molecules and the Cu surface (*SI Appendix*, Fig. S17), molecular assembly can be facilitated near the Cu@G NPs (Fig. 4*A*). Favorable π–π interactions allow both IR-140 and DCM molecules to lie flat on graphene (Fig. 4*B*); the adhesion energy of IR-140 on graphene (147 kcal/mol) is about 1.5 times that of DCM (93 kcal/mol). Calculations for dye molecules with different numbers of aromatic rings had adhesion energies that correlated linearly with the number of aromatic rings parallel to graphene (*SI Appendix*, Figs. S18–S20). These ring-number–dependent adhesion energies demonstrate that π–π interactions can facilitate the assembly of aromatic molecules near the Cu@G NPs.

To investigate the effects of molecular arrangement on the lasing response, we constructed a model of Cu@G NPs with a

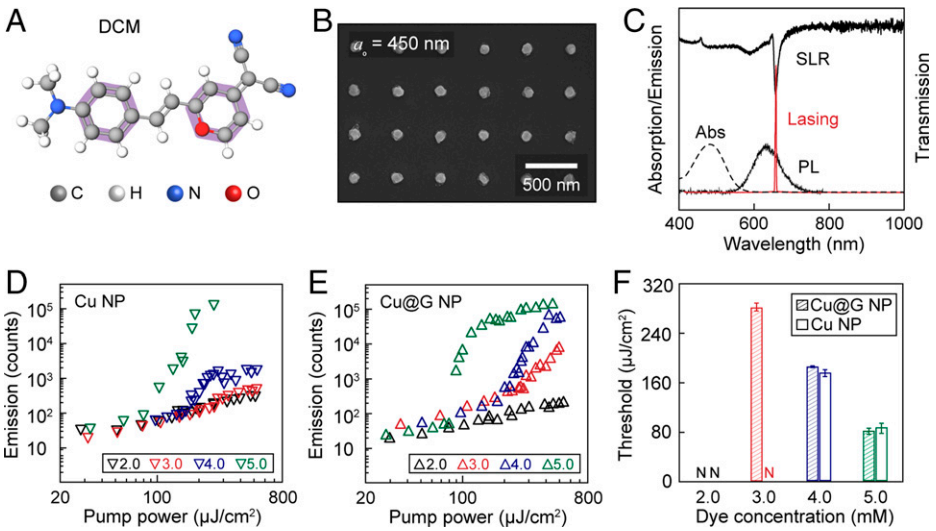

Fig. 3. Graphene coating leads to lasing modification of DCM in Cu NP lattices. (*A*) Three-dimensional ball-and-stick structure of a DCM molecule. Purple highlights aromatic rings in the same plane. (*B*) SEM image of Cu@G NP lattices with a_0 = 450 nm. (*C*) Absorption and PL of DCM in DMSO. SLR spectrally overlaps with PL to generate lasing at a wavelength of 650 nm. Lasing light-light curves of (*D*) annealed Cu and (*E*) Cu@G NP lattices at various DCM concentrations on the log-log scale. (*F*) Histogram of thresholds in the light-light curves for both lattices at various DCM concentrations. Error bars indicate the SD.

thin (2 nm) surface-dye layer containing a dye concentration higher (2.5 times) than the surrounding bulk solution (Fig. 4*C*). The thickness and concentration of the surface-dye layer were based on estimates of molecules assembled on graphene (41, 42). We performed finite-difference time-domain (FDTD) simulations for lasing with a series of dye concentrations. Concentration-dependent thresholds were observed in the light-light input-output curves for both Cu@G NP lattices (Fig. 4*C*) and Cu NP lattices (*SI Appendix*, Fig. S21). The two types of lattices had similar thresholds when the bulk concentrations were between 0.3 and 1 mM (Fig. 4*D*). Cu@G NP lattices showed lower thresholds than Cu NP lattices at 0.2 mM dye solutions, but no lasing was observed at 0.1 mM for both lattices. The simulated thresholds are consistent with experimental trends at different dye concentrations, which supports our hypothesis that local molecular assembly on the graphene surface can contribute to lower thresholds. Also, we expect that few-layer graphene can reduce quenching by 1)

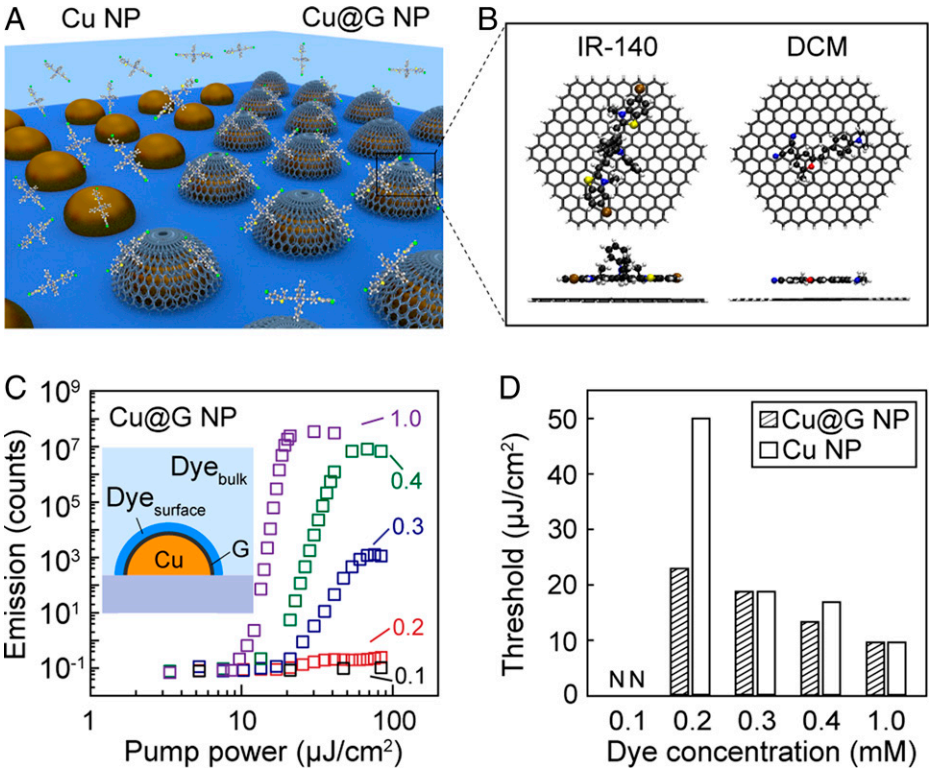

Fig. 4. Simulated lasing from Cu@G NP lattices. (*A*) Scheme of IR-140 molecules in DMSO around bare Cu NP (*Left*) and Cu@G NP (*Right*) in lattices. (*B*) DFT calculations of the IR-140 and DCM dye molecules on graphene. The calculated adhesion energies of IR-140 and DCM on graphene are 147 and 93 kcal/mol, respectively. (*C*) Simulated lasing light-light curves from Cu@G NP at different IR-140 concentrations. The colored numbers are bulk concentrations with a unit of millimolars. The inset panel is the scheme of the surface-dye model. (*D*) Histogram of lasing thresholds of simulated lattices at various IR-140 concentrations.

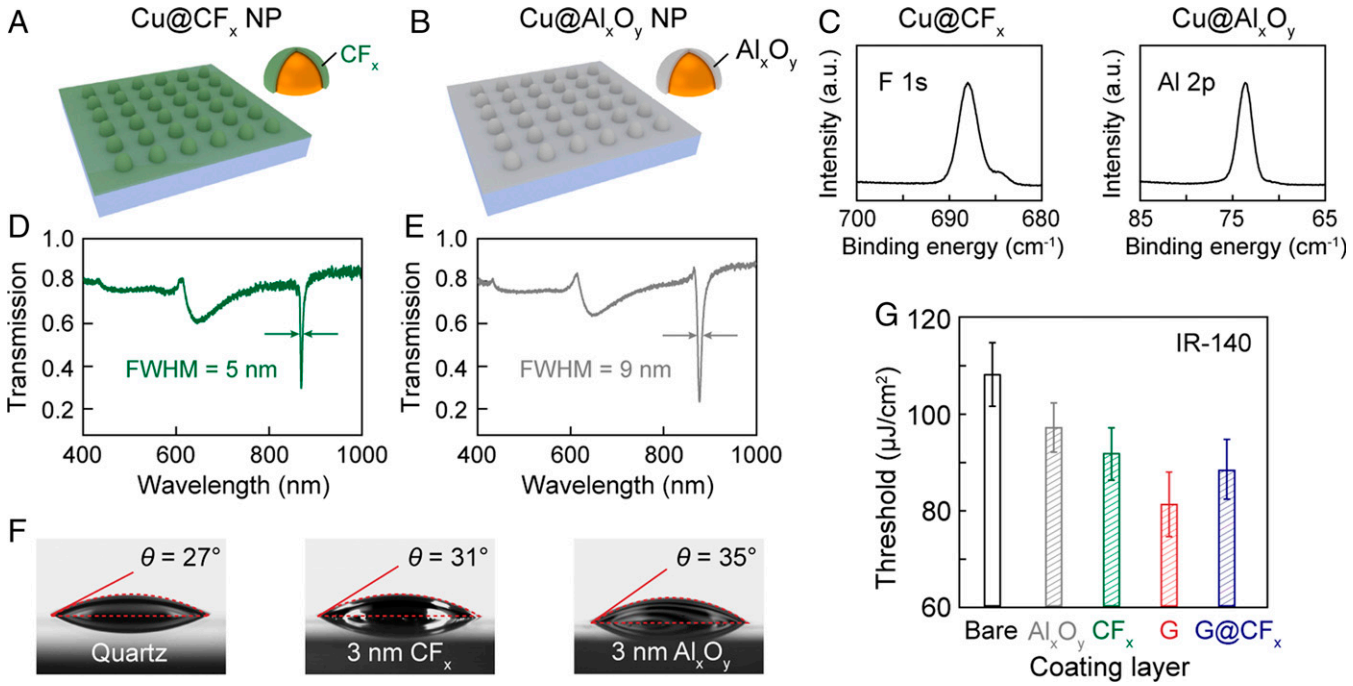

Fig. 5. Lasing from Cu NP lattices coated with dielectric layers. Schemes of (*A*) Cu@CF_x (green) and (*B*) Cu@Al_xO_y (gray) NP lattices. (*C*) XPS spectra of the F 1s peak from Cu@CF_x NP lattices and Al 2p peak from Cu@Al_xO_y NP lattices. Label a.u. stands for arbitrary unit.Transmission spectra of (*D*) Cu@CF_x and (*E*) Cu@Al_xO_y NP lattices with a_0 = 600 nm using DMSO as superstrate. The thickness of both dielectrics is 3 nm. (*F*) Contact angles of DMSO on quartz with 3-nm dielectric layers. (*G*) Histogram of lasing thresholds with different surface layers on Cu NP lattices. The G@CF_x represents 3-nm CF_x coating on Cu@G NPs. Gain media are 0.4 mM IR-140 in DMSO. Error bars indicate the SD.

functioning as a spacer layer between the dye and Cu NP surface and 2) suppressing nonradiative energy transfer due to n-doping effects (43) from energetic electron injection (*SI Appendix*, Fig. S22).

To differentiate between π–π interaction contributions and reduced quenching from graphene thickness on the improved lasing characteristics in Cu@G NP lattices, we compared lasing from Cu NP lattices covered with dielectric interfacial layers. CF_x and Al_xO_y were conformally coated with subnanometer precision using a CHF_3 plasma reactive-ion etching reaction (44) and atomic layer deposition (45), respectively (Fig. 5 *A* and *B*). First, we deposited the same thickness of CF_x or Al_xO_y as few-layer graphene (~3 nm) on annealed Cu NP lattices (*SI Appendix*, *SI Methods*). The layer composition was verified by the F 1s and Al 2p peaks in the X-ray photoelectron spectroscopy (XPS) spectra (Fig. 5*C*). These dielectric layers also provided sufficient protection against oxidation of the Cu NPs, and no CuO_x was detected (*SI Appendix*, Fig. S23). Compared to SLRs supported in bare Cu NP lattices, the CF_x layer did not change the transmission spectra, but the Al_xO_y layer broadened the SLR linewidth slightly (full width at half maximum [FWHM] from 5 to 9 nm) (Fig. 5 *D* and *E*). Different from the Cu@G NP lattices, these layers were uniformly coated on the entire surface because of a lack of selectivity between Cu and quartz. The CF_x and Al_xO_y layers had only nominal effects on the DMSO wetting contact angles on quartz (Fig. 5*F*), which indicates that molecular access near the NPs was unaffected by the coatings.

Using Cu@CF_x NP and Cu@Al_xO_y NP lattices (a_0 = 600 nm) as cavities, we performed lasing tests with IR-140 solutions (0.4 mM) (*SI Appendix*, Figs. S24 and S25). Both dielectric layers resulted in lower thresholds compared to bare Cu NPs because of suppressed quenching by the spatial separation of molecules from the NP surfaces (Fig. 5*G*). Notably, both coatings resulted in higher thresholds than few-layer graphene on Cu NP lattices, which indicates that the graphene functions as more than just a spacer layer. The increased thresholds of Cu@G NP lattices after coating an additional CF_x layer (purple bin in Fig. 5*G*) additionally confirmed the importance of π–π interactions from the graphene surface. Also, the lower thresholds of Cu NP lattices with CF_x coatings compared with Al_xO_y coatings suggest that lasing modifications from these dielectric layers are not identical (Fig. 5*G*). For 3-nm thicknesses, weak CF_x-dye attraction between F atoms and the electron-deficient aromatic thiazole ring in IR-140 could partially contribute to this difference (46, 47).

Compared to the self-limited thickness of graphene on Cu from the CVD process (48–50), CF_x and Al_xO_y layers with arbitrary thicknesses can be accurately deposited on NP lattices (44, 45). Even as the CF_x layer thickness increased, the FWHM, peak position, and intensity of the SLRs were retained. However, the Al_xO_y layer broadened the SLRs and shifted the peak to longer wavelengths (*SI Appendix*, Fig. S26). Fig. 6*A* depicts schemes of NP lattices with different thicknesses of CF_x or Al_xO_y layers in IR-140 solutions. Lasing spectra were collected from these devices (*SI Appendix*, Figs. S27–S30), and thicker Al_xO_y layers increased the lasing thresholds of Cu@Al_xO_y NP lattices, while Cu@CF_x NP lattices had similar thresholds as the thickness of CF_x increased (Fig. 6*B*). We performed FDTD simulations for lasing from dielectric-coated NP lattices with IR-140 (*SI Appendix*, Figs. S31–S33). Simulated thresholds were consistent with experimental trends, but there was no lasing emission with a 25-nm Al_xO_y coating (Fig. 6*C*).

Simulated electric field intensity maps of Cu@CF_x and Cu@Al_xO_y NP lattices with different dielectric coating thicknesses revealed further insight (*SI Appendix*, *SI Methods*). As the CF_x layer thickness increased, the electromagnetic near fields around the Cu NPs showed little modification (Fig. 6*D*); however, thicker Al_xO_y layers reduced both the intensity and the extent of the fields (Fig. 6*E*), which reduces the effective

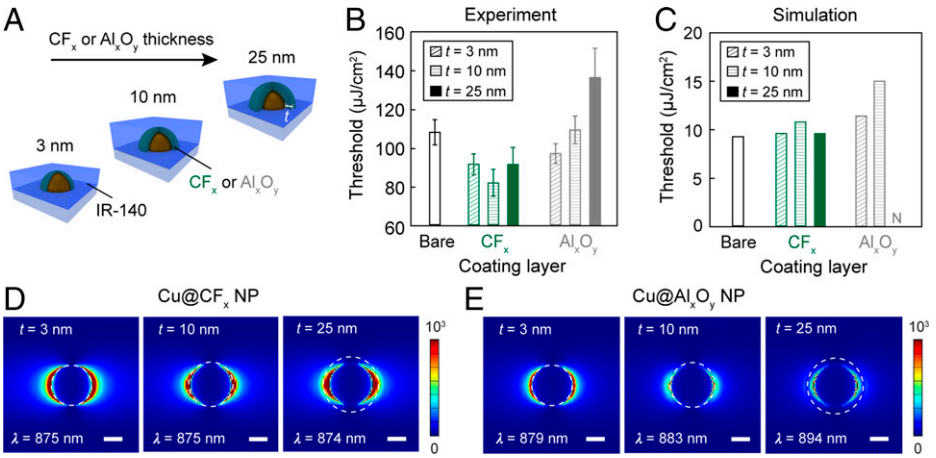

Fig. 6. Lasing from NP lattices with different thicknesses of dielectric layers. (*A*) Scheme of NP lattices with different thicknesses of CF_x or Al_xO_y layers in IR-140 solutions. Histogram of (*B*) experimental and (*C*) simulated lasing thresholds with different thickness of dielectric coating layers. Top view of the simulated field enhancement $|E|^2$ around a single NP in (*D*) Cu@CF_x and (*E*) Cu@Al_xO_y NP lattices. Scale bars are 50 nm. The thicknesses (*t*) of dielectric layers from *Left* to *Right* are 3, 10, and 25 nm. λ stands the resonance wavelength and white dashed circles mark the dielectric surfaces. Refractive indices for DMSO and substrate are 1.45 in simulations. Error bars indicate the SD.

interaction volume for molecular excitation. These materials-dependent near fields are due to refractive index differences in the dielectric surface layers. The CF_x layer has a similar refractive index ($n = 1.38$) to that of the surroundings ($n = 1.45$ for both DMSO and substrate), while the Al_xO_y layer, with its higher refractive index ($n = 1.76$ at 860 nm), starts to support waveguide effects with increased thickness and reduced field enhancements near the NPs.

In conclusion, we demonstrated precise control over the interfacial properties of plasmonic NP lattices that can affect lasing thresholds. Interfacial engineering was achieved by coating nanothin surface layers on plasmonic NPs, which tuned chemical interactions, refractive index, and spatial separation between the NP surface and the dye molecules. This strategy of tailoring specific interfacial interactions between plasmonic metasurfaces and excitonic materials is expected to advance both sensing and imaging applications that exploit selective emission enhancements. We believe that hybrid plasmonic metasurfaces with customizable surfaces will open prospects for programmable light-matter interactions on the nanoscale.

Materials and Methods

Cu NP lattices were fabricated with a soft nanofabrication process known as PEEL. Chemical vapor deposition and annealing treatment of Cu NP lattices were conducted in a quartz tube of a home-built, low-pressure chemical vapor deposition MTI system. The CF_x and Al_xO_y layers were coated through CHF_3 plasma reactive-ion etching and atomic layer deposition processes, respectively. The lasing measurements were performed at room temperature with a transverse electric (TE)-polarized fs-pulsed excitation source. Commercial software (FDTD Solutions, Lumerical Inc., Vancouver, BC, Canada) was used to simulate the optical properties of Cu NP lattices and lasing action. DFT simulations were used to calculate the adhesion energies between graphene and dye molecules.

Detailed information for the fabrication of Cu NP lattices, chemical vapor deposition for Cu@G NP lattices, annealing treatment for Cu NP lattices, CF_x and Al_xO_y layer coating on Cu NP lattices, lasing measurements, FDTD simulations, and DFT simulations can be found in *SI Appendix*.

Data Availability. All data are included in the article and/or *SI Appendix*.

ACKNOWLEDGMENTS. This work was supported by the Vannevar Bush Faculty Fellowship from the US Department of Defense (DOD N00014-17-1-3023). S.D. thanks the Cottrell Fellowship from the Research Corporation for Science Advancement (27464) and the National Science Foundation (CHE-2039044). G.K. and G.C.S. (electronic structure theory) were supported by the Department of Energy, Office of Basic Energy Sciences, under Grant DE-SC0004752. This work used the Northwestern University Micro/Nano Fabrication Facility, which is partially supported by the Soft and Hybrid Nanotechnology Experimental (SHyNE) Resource (NSF ECCS-1542205), the Materials Research Science and Engineering Center (DMR-1720139), the State of Illinois, and Northwestern University. Samples were characterized using the Electron Probe Instrumentation Center and Scanned Probe Imaging and Development facilities of Northwestern University's Atomic and Nanoscale Characterization Experimental Center, which has received support from the SHyNE Resource; the Materials Research Science and Engineering Center program (NSF DMR-1121262) at the Materials Research Center; the International Institute for Nanotechnology (IIN); the Keck Foundation; and the State of Illinois through the IIN. The CVD treatments were conducted at the Berry Research Laboratory at the University of Illinois Chicago.

1. N. Meinzer, W. L. Barnes, I. R. Hooper, Plasmonic meta-atoms and metasurfaces. *Nat. Photonics* **8**, 889–898 (2014).
2. A. Vaskin, R. Kolkowski, A. F. Koenderink, I. Staude, Light-emitting metasurfaces. *Nanophotonics* **8**, 1151–1198 (2019).
3. C. Li *et al.*, Dielectric metasurfaces: From wavefront shaping to quantum platforms. *Prog. Surf. Sci.* **95**, 100584 (2020).
4. Q. Zhao, J. Zhou, F. Zhang, D. Lippens, Mie resonance-based dielectric metamaterials. *Mater. Today* **12**, 60–69 (2009).
5. A. I. Kuznetsov, A. E. Miroshnichenko, M. L. Brongersma, Y. S. Kivshar, B. Luk'yanchuk, Optically resonant dielectric nanostructures. *Science* **354**, aag2472 (2016).
6. T. Liu, R. Xu, P. Yu, Z. Wang, J. Takahara, Multipole and multimode engineering in Mie resonance-based metastructures. *Nanophotonics* **9**, 1115–1137 (2020).
7. W. L. Barnes, A. Dereux, T. W. Ebbesen, Surface plasmon subwavelength optics. *Nature* **424**, 824–830 (2003).
8. S. A. Maier *et al.*, Local detection of electromagnetic energy transport below the diffraction limit in metal nanoparticle plasmon waveguides. *Nat. Mater.* **2**, 229–232 (2003).
9. N. I. Zheludev, S. L. Prosvirnin, N. Papasimakis, V. A. Fedotov, Lasing spaser. *Nat. Photonics* **2**, 351–354 (2008).
10. J. A. Schuller *et al.*, Plasmonics for extreme light concentration and manipulation. *Nat. Mater.* **9**, 193–204 (2010).
11. S. Zou, G. C. Schatz, Silver nanoparticle array structures that produce giant enhancements in electromagnetic fields. *Chem. Phys. Lett.* **403**, 62–67 (2005).
12. V. G. Kravets, A. V. Kabashin, W. L. Barnes, A. N. Grigorenko, Plasmonic surface lattice resonances: A review of properties and applications. *Chem. Rev.* **118**, 5912–5951 (2018).
13. D. Wang, W. Wang, M. P. Knudson, G. C. Schatz, T. W. Odom, Structural engineering in plasmon nanolasers. *Chem. Rev.* **118**, 2865–2881 (2018).
14. S. Deng *et al.*, Ultranarrow plasmon resonances from annealed nanoparticle lattices. *Proc. Natl. Acad. Sci. U.S.A.* **117**, 23380–23384 (2020).
15. S. Deng, B. Zhang, P. Choo, P. J. M. Smeets, T. W. Odom, Plasmonic photoelectrocatalysis in copper-platinum core-shell nanoparticle lattices. *Nano Lett.* **21**, 1523–1529 (2021).
16. W. Zhou *et al.*, Lasing action in strongly coupled plasmonic nanocavity arrays. *Nat. Nanotechnol.* **8**, 506–511 (2013).
17. S. I. Azzam *et al.*, Ten years of spasers and plasmonic nanolasers. *Light Sci. Appl.* **9**, 90 (2020).
18. R.-M. Ma, R. F. Oulton, Applications of nanolasers. *Nat. Nanotechnol.* **14**, 12–22 (2019).
19. D. Wang, J. Guan, J. Hu, M. R. Bourgeois, T. W. Odom, Manipulating light-matter interactions in plasmonic nanoparticle lattices. *Acc. Chem. Res.* **52**, 2997–3007 (2019).

20. Y. Lin *et al.*, Engineering symmetry-breaking nanocrescent arrays for nanolasing. *Adv. Funct. Mater.* **29**, 1904157 (2019).
21. D. Wang *et al.*, Band-edge engineering for controlled multi-modal nanolasing in plasmonic superlattices. *Nat. Nanotechnol.* **12**, 889–894 (2017).
22. R. Li *et al.*, Hierarchical hybridization in plasmonic honeycomb lattices. *Nano Lett.* **19**, 6435–6441 (2019).
23. A. Yang *et al.*, Real-time tunable lasing from plasmonic nanocavity arrays. *Nat. Commun.* **6**, 6939 (2015).
24. R. Guo, T. K. Hakala, P. Törmä, Geometry dependence of surface lattice resonances in plasmonic nanoparticle arrays. *Phys. Rev. B* **95**, 155423 (2017).
25. P. Anger, P. Bharadwaj, L. Novotny, Enhancement and quenching of single-molecule fluorescence. *Phys. Rev. Lett.* **96**, 113002 (2006).
26. S. Kühn, U. Håkanson, L. Rogobete, V. Sandoghdar, Enhancement of single-molecule fluorescence using a gold nanoparticle as an optical nanoantenna. *Phys. Rev. Lett.* **97**, 017402 (2006).
27. M. P. Knudson *et al.*, Polarization-dependent lasing behavior from low-symmetry nanocavity arrays. *ACS Nano* **13**, 7435–7441 (2019).
28. X. Meng, K. Fujita, S. Murai, T. Matoba, K. Tanaka, Plasmonically controlled lasing resonance with metallic-dielectric core-shell nanoparticles. *Nano Lett.* **11**, 1374–1378 (2011).
29. H. Chen *et al.*, Plasmon–molecule interactions. *Nano Today* **5**, 494–505 (2010).
30. R. Chikkaraddy *et al.*, Mapping nanoscale hotspots with single-molecule emitters assembled into plasmonic nanocavities using DNA origami. *Nano Lett.* **18**, 405–411 (2018).
31. X. Zhou *et al.*, Two-color single hybrid plasmonic nanoemitters with real time switchable dominant emission wavelength. *Nano Lett.* **15**, 7458–7466 (2015).
32. M. Ha *et al.*, Multicomponent plasmonic nanoparticles: From heterostructured nanoparticles to colloidal composite nanostructures. *Chem. Rev.* **119**, 12208–12278 (2019).
33. D. Ge *et al.*, Hybrid plasmonic nano-emitters with controlled single quantum emitter positioning on the local excitation field. *Nat. Commun.* **11**, 3414 (2020).
34. A. Biswas *et al.*, Advances in top-down and bottom-up surface nanofabrication: Techniques, applications & future prospects. *Adv. Colloid Interface Sci.* **170**, 2–27 (2012).
35. M. H. Lee, M. D. Huntington, W. Zhou, J.-C. Yang, T. W. Odom, Programmable soft lithography: Solvent-assisted nanoscale embossing. *Nano Lett.* **11**, 311–315 (2011).
36. J. Henzie, M. H. Lee, T. W. Odom, Multiscale patterning of plasmonic metamaterials. *Nat. Nanotechnol.* **2**, 549–554 (2007).
37. V. Georgakilas *et al.*, Noncovalent functionalization of graphene and graphene oxide for energy materials, biosensing, catalytic, and biomedical applications. *Chem. Rev.* **116**, 5464–5519 (2016).
38. V. Georgakilas *et al.*, Functionalization of graphene: Covalent and non-covalent approaches, derivatives and applications. *Chem. Rev.* **112**, 6156–6214 (2012).
39. S.-L. Chua *et al.*, Modeling of threshold and dynamics behavior of organic nanostructured lasers. *J. Mater. Chem. C Mater. Opt. Electron. Devices* **2**, 1463–1473 (2014).
40. P. Song *et al.*, Stable molecular diodes based on π-π interactions of the molecular frontier orbitals with graphene electrodes. *Adv. Mater.* **30**, 1706322 (2018).
41. J.-H. Deng *et al.*, π-π stacking interactions: Non-negligible forces for stabilizing porous supramolecular frameworks. *Sci. Adv.* **6**, eaax9976 (2020).
42. H. Fukunaga, H. Miyasaka, Magnet design by integration of layer and chain magnetic systems in a π-stacked pillared layer framework. *Angew. Chem. Int. Ed. Engl.* **54**, 569–573 (2015).
43. Z. Fang *et al.*, Plasmon-induced doping of graphene. *ACS Nano* **6**, 10222–10228 (2012).
44. M. D. Huntington, C. J. Engel, A. J. Hryn, T. W. Odom, Polymer nanowrinkles with continuously tunable wavelengths. *ACS Appl. Mater. Interfaces* **5**, 6438–6442 (2013).
45. S. M. George, Atomic layer deposition: An overview. *Chem. Rev.* **110**, 111–131 (2010).
46. P. Li *et al.*, Stabilizing fluorine-π interactions. *Angew. Chem. Int. Ed. Engl.* **56**, 7209–7212 (2017).
47. S. Guha, S. Saha, Fluoride ion sensing by an anion-π interaction. *J. Am. Chem. Soc.* **132**, 17674–17677 (2010).
48. X. Li *et al.*, Large-area synthesis of high-quality and uniform graphene films on copper foils. *Science* **324**, 1312–1314 (2009).
49. K. Yan, H. Peng, Y. Zhou, H. Li, Z. Liu, Formation of bilayer bernal graphene: Layer-by-layer epitaxy via chemical vapor deposition. *Nano Lett.* **11**, 1106–1110 (2011).
50. M. Huang *et al.*, Large-area single-crystal AB-bilayer and ABA-trilayer graphene grown on a Cu/Ni(111) foil. *Nat. Nanotechnol.* **15**, 289–295 (2020).